Low Temperature Physics/Fizika Nizkikh Temperatur, 2021, vol. 47, No. 7, pp. 613–625

Electronic structure and physical properties of hybrid heterostructures $Sr_2CrOsO_6/BaTiO_3$

V. N. Antonov and L. V. Bekenov

G. V. Kurdyumov Institute for Metal Physics of the National Academy of Sciences of Ukraine, Kyiv 03142, Ukraine
E-mail: antonov@imp.kiev.ua

Received January 13, 2021, published online May 26, 2021

We report on the electronic structure and magnetic properties of hybrid heterostructures combined the ferromagnetic double perovskite Sr_2CrOsO_6 (SCOsO) and ferroelectric $BaTiO_3$ (BTO) calculated in the GGA approach using the fully relativistic spin-polarized Dirac LMTO method. The electronic band structure is studied in the BTO and SCOsO oxides as well as in SCOsO/BTO heterostructures with different supercells: (1×1×1) monolayered, (2×2×1), and (1×1×2) SCOsO/BTO heterostructures. The optical and magneto-optical spectra of pure BTO and SCOsO oxides as well as of the SCOsO/BTO heterostructures are investigated theoretically and compared with avaliable experimental data. The element-specific x-ray absorption spectra as well as the x-ray magnetic circular dichroism at the Ti, Ba, and Os $L_{2,3}$ edges in SCOsO/BTO heterostructures are investigated theoretically. Good agreement with experimental spectra has been found.

Keywords: electronic structure, magnetic moment, x-ray magnetic circular dichroism, dielectric function, Kerr rotation, heterostructures, multiferroics.

1. Introduction

Materials with multiple simultaneous electric and magnetic ordering attract much attention in recent years. The phenomena of ferroelectricity and ferromagnetism derive from the fact that the electrons possess charge and spin, hence, a material may have an electric or magnetic polarization. A few materials possess both ferroelectric and magnetic polarizations in the same phase with a coupling between them. These materials are called multiferroics and possess the so called magneto-electric (ME) effect [1, 2]. Multiferroics provide novel device concepts, which have recently become of great interest to researchers from the application point of view [3–6]. Besides, the fundamental physics of multiferroic materials is very fascinating.

Unfortunately, the number of multiferroics offering a perspective for applications is quite rare. A key reason for this limited set is the fact that the two order parameters have exactly the opposite requirements in terms of the electronic structure. Typically, ferromagnetism (especially in metallic systems) is related to the ordering of spins of electrons in incomplete ionic shells, that is, it results from partially filled *d* orbitals and requires the kinetic energy of the electron to be dominant; on the other hand, ferroelectricity results from relative shifts of negative and positive ions that induce surface charges, usually it requires formally empty *d* orbitals and a perfectly insulating state. For this reason, in a single-phase multiferroics, the effect is often very weak, and multiple ordering occurs only at low temperatures for most materials. As a result, potential applications have not been realized yet. In fact, $BiFeO_3$ is the only room temperature multiferroic (antiferromagnetic and ferroelectric) so far, which has attracted great interest and extensive studies in the past decade [7].

Besides the search and synthesis of single-phase multiferroics, much effort in past decade has been made to synthesis heterostructures composed of materials that have large ferromagnetic (FM) and ferroelectric (FE) ordering, with the possibility of ME coupling. Several configurations have been employed to fabricate ME composite thin films: composites with FE or FM terminal layers, multilayer nanostructures, superlattice structures with alternate FM and FE layers and epitaxial ferroelectromagnetic nanocomposites fabricated by self-assembly technique. These nanostructured thin films have been found to exhibit a larger ME effect than that of the single-phase materials by more than one order of magnitude [8]. A new level in design and development in multiferroic thin films has been achieved due to improved first-principles computational techniques. The advancement of both experimental fabrication processes and theoretical modeling codes and parallel processing among theoretical and experimental scientists has aided in the design of new magnetoelectrics with larger coupling parameters [9, 10].

© V. N. Antonov and L. V. Bekenov, 2021

Most technologically important ferroelectrics such as $BaTiO_3$ (BTO) and (Pb, Zr)TiO_3 are transition metal oxides with the perovskite (ABO_3) structure. They have a cubic structure at high temperature with a small B-site cation at the center of an octahedral cage of oxygen ions and a large A-site cation at the unit cell corners. In parallel, there is a large number of ferrites with the spinel structure (AB_2O_4) [11]. Recently, there have been reports on $CoFe_2O_4/BaTiO_3$, $SrRuO_3/BaTiO_3$, $La_{0.67}Sr_{0.33}MnO_3/BaTiO_3$, and $Fe_3O_4/BaTiO_3$ hybrids [12–17]. They show a magnetoelectric coupling effect, manifesting itself as a change in the magnetization and resistance of the ferromagnetic thin film at the structural phase transition temperatures of $BaTiO_3$. Another promising materials are the ferromagnetic double perovskites (DP) $A_2BB'O_6$ (A = alkaline earth or rare earth and BB′ are heterovalent transition metals such as B = Fe, Cr, Mn, Co, Ni; B′ = Mo, Re, W, Os) [18, 19]. They often demonstrate intrinsically complex magnetic structures and a wide variety of physical properties as a consequence of the strong interplay between structure, charge and spin ordering [20] (see Ref. 21 for a review article on these materials). In particular, the series $Sr_2CrB'O_6$ with B′ being W, Re, and Os ions is very promising due to their record high values of T_c (T_c = 500 K and 635 K for B′ = W and Re, respectively) [22, 23]. Sr_2CrOsO_6 has an even higher ordering temperature T_c = 725 K, the highest known in this class, and was reported to be an insulator [24].

Artificial oxide heterostructures are particularly promising for the realization of materials with improved and new functionalities and novel device concepts. Nano-structuring is a promising approach that has opened the door to the design of practical devices based on the ME coupling. Thin film multiferroics are beginning to reveal a range of fascinating phenomena as well as to stimulate the exploration of new device heterostructures, which have potential applications in microdevices and integrated units such as microsensors, microelectromechanical systems devices and high density information storage. Hereby, interface and surface effects play a crucial role. Due to the complexity of the involved oxide materials, the rich variety of physics resulting from band bending effects, magnetic exchange, or elastic coupling at interfaces in heterostructures is far from being understood and needs further detailed studies. Moreover, intermixing of the different atomic species deposited in multilayer structures plays an important role and might influence or even dominate the overall physical properties. Therefore, a careful investigation of the electronic structure of artificial material systems is highly necessary.

The aim of this work is the detailed theoretical investigations of the electronic structure, the optical and magneto-optical (MO) properties as well as x-ray magnetic circular dichroism (XMCD) in SCOsO/BTO heterostructures. The energy band structure of these heterostructures is calculated within the ab initio approach using the fully relativistic spin-polarized Dirac linear-muffin-tin-orbital (LMTO) method.

The paper is organized as follows. The computational details are presented in Sec. 2. Section 3 presents the electronic structure of BTO, SCOsO and the SCOsO/BTO heterostructures. Section 4 is devoted to the theoretical calculations of the optical and MO properties, x-ray absorption spectra (XAS) and XMCD. Theoretical results are compared to the experimental measurements. Finally, the results are summarized in Sec. 5.

2. Computational details

2.1. Magneto-optical effects

MO effects refer to various changes in the polarization state of light upon interaction with materials possessing a net magnetic moment, including rotation of the plane of linearly polarized light (Faraday, Kerr rotation), and the complementary differential absorption of left and right circularly polarized light (circular dichroism). In the near visible spectral range these effects result from excitation of electrons in the conduction band. Near x-ray absorption edges, or resonances, magneto-optical effects can be enhanced by transitions from well-defined atomic core levels to transition symmetry selected valence states.

For a crystal of cubic symmetry, where the magnetization $\mathbf{M}$ is parallel to the z-axis, the dielectric tensor is composed of the diagonal ε_{xx} and ε_{zz} and the off-diagonal ε_{xy} components in the form

$$\varepsilon = \begin{pmatrix} \varepsilon_{xx} & \varepsilon_{xy} & 0 \\ -\varepsilon_{xy} & \varepsilon_{xx} & 0 \\ 0 & 0 & \varepsilon_{zz} \end{pmatrix}. \tag{1}$$

A complete description of the MO effects is given by the four nonzero elements of the dielectric tensor or, equivalently, by the complex refractive index $n(\omega)$

$$n(\omega) \equiv \sqrt{\varepsilon(\omega)} = 1 - \delta(\omega) + i\beta(\omega) \tag{2}$$

for several normal modes corresponding to the propagation of pure polarization states along specific directions in the sample, which can be obtained by solving Maxwell's equations [25]. Two of these modes are for circular components of opposite ($\pm$) helicity with the wave vector $\mathbf{h} \parallel \mathbf{M}$ and have indices

$$n_{\pm} = 1 - \delta_{\pm} + i\beta_{\pm} = \sqrt{\varepsilon_{xx} \pm i\varepsilon_{xy}}\,. \tag{3}$$

The other two modes are for linear polarizations with $\mathbf{h} \perp \mathbf{M}$ [26]. One has the electric vector $\mathbf{E} \parallel \mathbf{M}$ and index $n_{\parallel} = 1 - \delta_{\parallel} + i\beta_{\parallel} = \sqrt{\varepsilon_{zz}}$. The other has $\mathbf{E} \perp \mathbf{M}$ and $n_{\perp} = 1 - \delta_{\perp} + i\beta_{\perp} = \sqrt{(\varepsilon_{xx}^2 + \varepsilon_{xy}^2)/\varepsilon_{xx}}$.

The x-ray magnetic circular dichroism is given by $\beta_+ - \beta_-$ and is first order in M. Magnetic linear dichroism $n_{\perp} - n_{\parallel}$ (also known as the Voigt effect) is quadratic in M. The Voigt effect is present in both ferromagnets and antiferromagnets, while the first order MO effects in the forward scattering beam are absent with the net magnetization in antiferromagnets.

Within the one-particle approximation, the absorption coefficient $\mu_j^{\lambda}(\omega)$ for incident x-ray of polarization λ and photon energy $\hbar\omega$ can be determined as the probability of electronic transitions from initial core states with the total angular momentum j to final unoccupied Bloch states

$$\mu_{\lambda}^{j}(\omega) =$$

$$= \sum_{m_j}\sum_{n\mathbf{k}} \left| \left\langle \Psi_{n\mathbf{k}} \left| \Pi_{\lambda} \right| \Psi_{jm_j} \right\rangle \right|^2 \delta\left(E_{n\mathbf{k}} - E_{jm_j} - \hbar\omega\right) \theta\left(E_{n\mathbf{k}} - E_F\right), \tag{4}$$

where Ψ_{jm_j} and E_{jm_j} are the wave function and the energy of a core state with the projection of the total angular momentum m_j; $\Psi_{n\mathbf{k}}$ and $E_{n\mathbf{k}}$ are the wave function and the energy of a valence state in the nth band with the wave vector $\mathbf{k}$; E_F is the Fermi energy.

Π_{λ} is the electron-photon interaction operator in the dipole approximation

$$\Pi_{\lambda} = -e\boldsymbol{\alpha}\, \mathbf{a}_{\lambda}, \tag{5}$$

where $\boldsymbol{\alpha}$ are the Dirac matrices, $\mathbf{a}_{\lambda}$ is the λ polarization unit vector of the photon vector potential, with $a_{\pm} = 1/\sqrt{2}(1, \pm i, 0)$, $a_{\parallel} = (0, 0, 1)$. Here, + and − denotes, respectively, left and right circular photon polarizations with respect to the magnetization direction in the solid. Then, x-ray magnetic circular and linear dichroisms are given by $\mu_+ - \mu_-$ and $\mu_{\parallel} - (\mu_+ + \mu_-)/2$, respectively. More detailed expressions of the matrix elements for the spin-polarized fully relativistic LMTO method may be found in Refs. 27, 28.

2.2. Structural models

Barium titanate is the prototype ferroelectric. Its crystallographic structure shows a variety of phase transitions, dependent on the temperature [29, 30]. Above 393 K, bulk BTO is cubic [$Pm\bar{3}m$; group number 221, see Fig. 1(b)] and paraelectric. Below 393 K, it becomes ferroelectric and its lattice structure changes to tetragonal ($P4/mmm$). Within the ferroelectric state, the lattice symmetry is further reduced to orthorhombic (below 278 K), and finally to rhombohedral (below 183 K). The dielectric constant, the spontaneous polarization, as well as the lattice constants change abruptly at these phase transition temperatures, accompanied by a thermal hysteresis [31].

The low temperature (2 K) phase of SCOsO is a rhombohedral double perovskite structure with the space group $R\bar{3}$, and returns to the cubic double perovskite structure ($Fm\bar{3}m$) at higher temperatures (500 K) [24].

Figure 1 shows three types of heterostructures used in our calculations: a monolayered (1×1×1) heterostructure, a (2×2×1) supercell heterostructure, and a (1×1×2) supercell heterostructure together with SCOsO and BTO crystal structures.

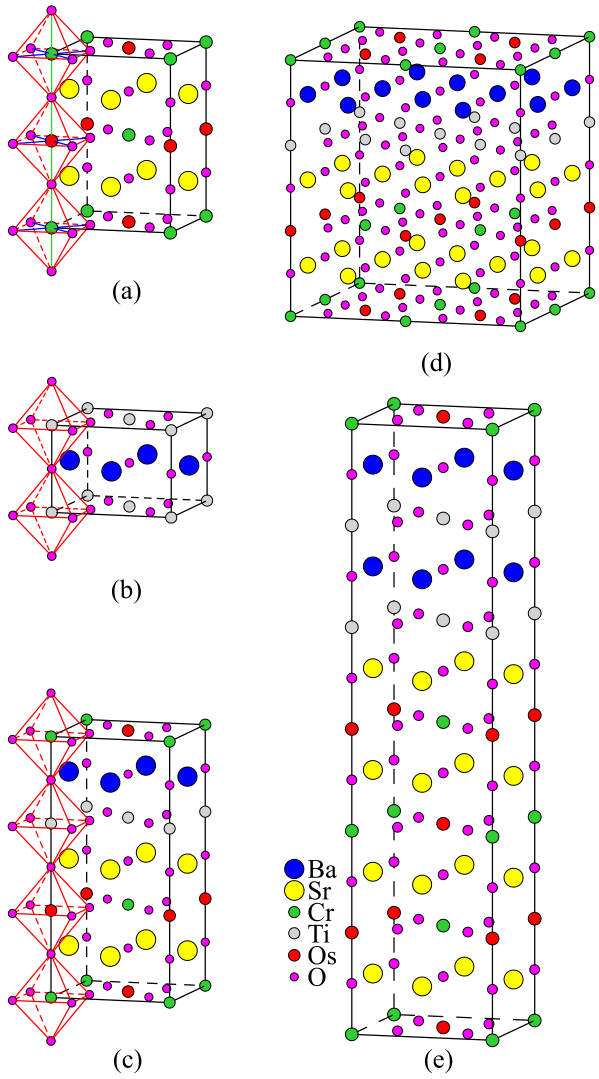

Fig. 1. (Color online) Schematic representations of the (a) $I4/m$ SCOsO structure; (b) $Pm\bar{3}m$ BTO structure; (c) $P4mm$ SCOsO/BTO monolayered (1×1×1) heterostructure; (d) $P4mm$ SCOsO/BTO (2×2×1) heterostructure; (e) $P4mm$ SCOsO/BTO (1×1×2) heterostructure.

2.3. Calculation details

The details of the computational method are described in our previous papers [32–38], and here we only mention some aspects specific to the present calculations. The calculations were performed using the spin-polarized fully relativistic LMTO method [39, 40] for the experimentally measured lattice parameters [30]. Our implementation of the LMTO method uses four-component basis functions constructed by solving the Dirac equation inside an atomic sphere [41]. The local spin-density approximation (LSDA) part of the calculations was based on the spin-density functional with the Perdew–Wang exchange-correlation potential [42]. The exchange-correlation functional of a GGA-type was also used in the version of Perdew, Burke,

and Ernzerhof [43]. The basis consisted of the s, p, and d LMTO's for O sites and empty spheres, the s, p, d, and f LMTO's for Ti, Cr, Sr, and Os sites, and the s, p, d, f, and g LMTO's for Ba sites. The **k**-space integrations were performed with the improved tetrahedron method [44]. We used $16\times16\times16$ division of the Brillouin zone (BZ). This corresponds to 4096 **k**-points in the irreducible part of BZ in SCOsO on BTO. The finite lifetime of a core hole was accounted for by folding the XAS and XMCD spectra with a Lorentzian. The widths of core levels were taken from Ref. 45. The finite experimental resolution of the spectrometer was accounted for by a Gaussian of 0.6 eV width.

In the x-ray absorption process an electron is promoted from a core level to an unoccupied state, leaving a core hole. As a result, the electronic structure at this state differs from that of the ground state. In order to reproduce the experimental spectrum the self-consistent calculations should be carried out including the core hole. In this study the core-hole effect was fully taken into account in the self-consistent iterations by removing an electron at the core orbital using the supercell approximation. The core state of the target atom in the ground state provides the initial state $|i\rangle$ for the spectral calculation. The final states $|f\rangle$ are the conduction band states obtained separately by the calculations in which one of the core electrons of the target atom is placed at the lowest conduction band. The interaction and the screening of the electron-hole pair are fully accounted for by the self-consistent iterations of the final state Kohn–Sham equations. This procedure simulates the experimental situation, in which the sample can easily supply an electron to screen a localized charge produced by the core hole. Such an approach considers the symmetry breaking of the system in a natural way, and self-consistently describes the charge redistribution induced by the core hole. A similar approximation has been used by several authors [46–52] for the interpretation of the x-ray absorption. However, the effect of the electron-hole interaction in the final state on the XMCD spectra has been investgated to a much lesser extent in the literature. One should mention that the effect of the electron-hole interaction in the final state is different for different edges and systems with different localization of the electronic states. For example, Ikeno and Mizoguchi [52] show that the proper introduction of the core-hole effect improves the agreement between the calculated and experimentally measured XAS at the oxygen K edge in MgO. Mo and Ching [48] obtained excellent agreement with experimental XAS for Si K, Si $L_{2,3}$, and O K edges in α-SiO2. The usual interpretation using the orbital-resolved local density of states in the conduction band was unsatisfactory. The final-state interaction improves the agreement between theory and experiment for the XMCD spectra at the Gd $M_{4,5}$ and N K edges in GdN, however, it has a minor influence on the shape of the Gd $L_{2,3}$ XMCD spectra [34]. We should mention also that the size of the supercell is important, and it should be large enough to inhibit the interaction between excited atoms in neighboring supercells. In our calculations we used a $2\times2\times2$ supercell. At one of the Ti (or Os and Ba) atoms we created a hole at the $2p_{1/2}$ or $2p_{3/2}$ levels separately for the self-consistent calculations of the L_2 and L_3 spectra, respectively.

It is well-known that the Kohn–Sham equation of DFT is described by a local potential which depends only on the electron spin density. The orbital current, which is responsible for the orbital magnetic moment M_l, is, however, not included into the equations. This means, that although the spin magnetic moment M_s is self-consistently determined in LSDA (GGA), there is no framework to determine simultaneously M_l self-consistently. Therefore, the LSDA (GGA) calculations fail to produce the correct value of the orbital moment of the elements with strong SO interaction, such as uranium compounds [53–58]. Numerous attempts have been made to solve that problem. They can be roughly classified into two categories. One is based on the so-called current density functional theory [59–61] which is intended to extend the density functional theory to include the orbital current as an extra degree of freedom, which describes M_l. Unfortunately an explicit form of the current density functional is at present unknown. The other category includes orbital polarization (OP) [54–57] and self-interaction corrections (SIC) [62], and LSDA+U [63, 64] approaches, which provide a means to calculate M_l beyond the LSDA (GGA) scheme. In our previous publication we show that to obtain an insulating ground state in SCOsO, one has to take into account the OP correction [65].

Solovyev *et al.* [63] argued that the key parameter responsible for the exchange-correlation enhancement of the orbital magnetic moments in solids is the "Hubbard U" rather than the intra-atomic Hund's second rule coupling, being consistent with a more general concept of the orbital polarization. This leads to a unified rotationally invariant LSDA+U prescription for the orbital magnetism [64]. This generalization of the LSDA+U method takes into account that in the presence of SO coupling the occupation matrix of localized electrons becomes nondiagonal in spin indexes [64]. The matrix elements of this method contain both $F^0 = U$, which provides the splitting of the localized states into "lower and upper Hubbard subbands", and the terms proportional to the Slater integrals F^2, F^4, and F^6, which are responsible for angular correlations within the localized shell. In the case when U is effectively screened and $U_{\text{eff}} = U - J$ becomes small, the latter terms give the dominant contribution to the corresponding matrix elements. In our GGA+U calculations we used $U = J = 0.8$ eV. In this case $U_{\text{eff}} = 0$ and the effect of the GGA+U comes from nonspherical terms which are determined by F^2, F^4, and F^6 Slater integrals. In the following we will refer to calculations performed using the GGA+U method with $U_{\text{eff}} = 0$ as GGA+OP calculations.

3. Electronic structure

Generally in 3*d* transition metal oxides (TMOs), the SO coupling is typically less than 0.05 eV. This is much smaller than other important energies in 3*d* TMOs, such as the on-site Coulomb interaction energy, U (3–5 eV), and the crystal-field splitting energy, Δ (2–3 eV). Therefore, the SO coupling is not dominant in determining the physical properties of 3*d* TMOs. On the other hand, in 5*d* TMOs the SO coupling is approximately 0.3–0.5 eV [66], and therefore should be taken into account [67].

Figure 2 presents the energy band structures of BTO, the SCOsO double perovskite, SCOsO/BTO, and $[SCOsO/BTO]_{1\times1\times2}$ heterostructures calculated in the fully relativistic Dirac approach. The energy band structure of SCOsO in spin polarized calculations without SO coupling possesses identical widths of occupied Os spin-down states and Cr spin-up t_{2g} manifolds of 1.8 eV [65]. The Cr spin moment is completely compensated by the Os, six O and two Sr spin moments. Therefore, first principles calculations predict that SCOsO is (without considering the SO coupling) actually a ferrimagnetic semimetal with precisely compensating spin moments, or a spin-asymmetric compensated semimetallic ferrimagnet in which the electrons and holes are each fully polarized and have opposite spin directions, in spite of a zero net moment and hence no macroscopic magnetic field. This is a peculiar state indeed. The SO coupling degrades this state by giving a nonzero total moment, but the band structure is little changed. Upon including the SO coupling, the Cr moment is almost unchanged, the Os spin moment is slightly reduced and an orbital moment is induced [65]. The total net moment of 0.545 μ_B reflecting both spin and orbital compensations is reasonably close to the measured saturation moment of 0.75 μ_B [24]. We can conclude that the observed saturation moment of ferrimagnetic SCOsO is entirely due to the spin-orbit coupling, and without this coupling SCOsO would be spin compensated (zero net moment). A similar picture is valid also for the SCOsO/BTO, $[SCOsO/BTO]_{1\times1\times2}$, and $[SCOsO/BTO]_{2\times2\times1}$ heterostructures. The spin polarized calculations produce a spin-asymmetric compensated ferrimagnet with no macroscopic magnetic field in which two Cr spin moments of 4.711 μ_B is completely compensated with two Os spin moments of –3.445 μ_B, nine oxygen spin moments of –1.182 μ_B, four Sr spin moments of –0.063 μ_B, two Ba spin moments of –0.013 μ_B, and two Ti spin magnetic moments of –0.008 μ_B (for the $[SCOsO/BTO]_{1\times1\times2}$ heterostructure). The total net moment is equal to 1.803 μ_B and 1.545 μ_B for the SCOsO/BTO and $[SCOsO/BTO]_{1\times1\times2}$ heterostructures, respectively.

The ground state band structure of SCOsO with the SO coupling has a semimetal character. To obtain the insulating ground state observed experimentally [24] one has to take into account the OP correction. We applied intra-atomic Coulomb repulsion U on the Os ion using the LSDA+SO+OP method (with $U_{\text{eff}} = U - J = 0$ eV) to obtain the insulating solution (see the middle panel in Fig. 2). Therefore, the opening of the gap in SCOsO is not such as in a Mott insulator (it is a band insulator), but rather as an "energy gap correction" to GGA. The GGA+SO+OP approach produces the insulating solution for SCOsO, and the SCOsO/BTO, $[SCOsO/BTO]_{1\times1\times2}$ heterostructures, however, the $[SCOsO/BTO]_{2\times2\times1}$ heterostructure is a semimetal with very small DOS at the Fermi level.

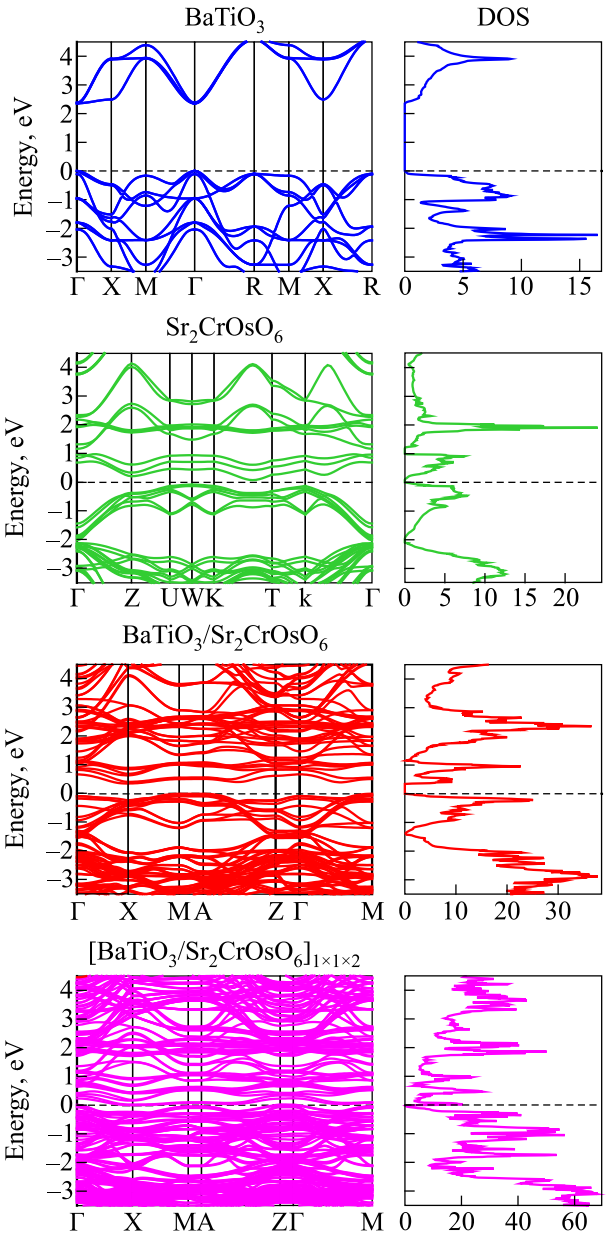

Fig. 2. (Color online) The energy band structure of BTO, the SCOsO double perovskite, SCOsO/BTO and SCOsO/BTO (1×1×2) heterostructures calculated in the GGA+SO+OP approximation.

The partial DOSs for the SCOsO/BTO heterostructure with the spin-orbit coupling and OP taking into account are presented in Fig. 3. The electronic energy bands between –19.5 eV and –16.5 eV are dominated by the O 2*s* states.

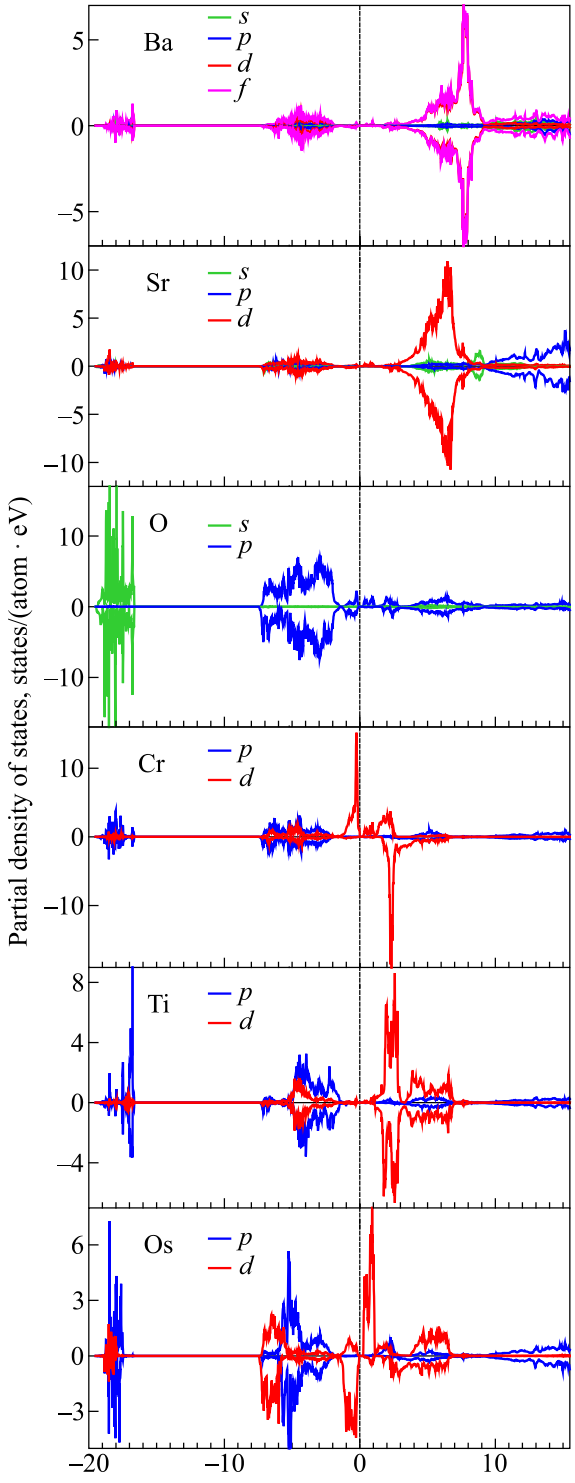

Fig. 3. (Color online) The partial DOSs [in states/(atom·eV)] of SCOsO/BTO calculated in the GGA+SO+OP spin-polarized approximation. The p partial DOSs of Cr, Ti, and, Os are multiplied by the factor of 10.

The O $2p$ states occupy mostly the –7.5 eV to –1.8 eV energy interval. Thre is a small amount of Ba $5d$ hybridized valence states from –2 eV to –6.5 eV. The Ba $4f$ empty states are situated from 3.5 eV to 9.5 eV above the Fermi level. The Sr $4d$ and $5p$ empty states above the Fermi level are situated from 3 eV to 7.5 eV and above 10 eV, respectively. The occupied Cr $3d$ spin-up states are at –1.4 eV to 0 eV, narrow spin-down Cr empty states are at 1.9 eV to 2.3 eV above the Fermi level. The energy states in the close vicinity of the Fermi level at the Os site are derived purely from the $x^2 - y^2$ and yz orbitals. Because of a smaller exchange splitting and the opposite spin magnetic moment direction (see Table 1) the Os $5d$ empty spin-up states are situated closer to the Fermi level than the corresponding Cr $3d$ states. The Os $6s$ states occupy two energy intervals from –17.2 eV to –19.7 eV and from –1.9 eV to –6 eV. Most of the Ti $3d$ states are empty. They are subdivided into two groups. The states occupying the 1 eV to 3.2 eV energy interval have $x^2 - y^2$ and yz characters. The high energy states from 3.4 eV to 7 eV consist of $3z^2 - 1$ and xy orbitals. The occupied Ti $3d$ states are situated from –2 eV to –5 eV below the Fermi level. The occupied Ti $4p$ states occupy two energy intervals from –16.6 eV to –18.7 eV and from –1.5 eV to –5 eV.

Table 1. The theoretically calculated and experimentally measured spin M_s and orbital M_l magnetic moments (in μ_B) at the Cr, Os, Ti, Sr, Ba, and O sites of the SCOsO double perovskite and SCOsO/BTO$_{1\times1\times1}$ heterostructure

Atom	Method	SCOsO		SCOsO/BTO	
		M_s	M_l	M_s	M_l
Cr	GGA+SO	2.289	–0.031	2.420	–0.047
	Sum rules	1.939	–0.024		
	Theory [24]	2.216	–0.024		
	Theory [68]	2.194	0.142		
	Theory [69]	2.21	–0.02		
Os	GGA+SO	–1.434	0.104	–1.548	0.105
	Sum rules	–1.236	0.103	–1.436	0.007
	Theory [24]	–1.214	0.122		
	Theory [68]	–1.312	0.173		
	Theory [69]	–1.32	0.11		
Ti	GGA+SO			–0.001	–0.002
Sr	GGA+SO	–0.031	–0.003	–0.013	–0.002
Ba	GGA+SO			–0.006	–0.001
O	GGA+SO	–0.085	–0.006	–0.048	0.005

In magnets, the spin M_s and orbital M_l magnetic moments are basic quantities and their separate determination is therefore important. The methods of their experimental determination include traditional gyromagnetic ratio measurements [70], magnetic form factor measurements using neutron scattering [71], and magnetic x-ray scattering [72]. In addition to these, the x-ray magnetic circular dichroism combined with several sum rules [73, 74] has attracted much attention as a method of site- and symmetry-selective determination of M_s and M_l. Table 1 presents the comparison between calculated and experimental magnetic moments at the Cr, Os, Ti, Ba, Sr, and O sites of the SCOsO double perovskite and SCOsO/BTO$_{1\times1\times1}$ heterostructure.

The Cr and Os spin and orbital moments are antiparallel in the SCOsO double perovskite and SCOsO/$BTO_{1\times1\times1}$ heterostructure, in accordance with Hund's third rule. In SCOsO the Cr spin moment of 2.289 μ_B as well as the orbital moment of –0.031 μ_B are in good agreement with previous calculations [24, 69]. Our Os spin magnetic moment in SCOsO is slightly larger and orbital moment is smaller than the results of Refs. 24, 68. The results from different calculations may vary somewhat since the calculated moments depend on the details of calculations and especially on the sizes of muffin-tin spheres, which usually differ from each other for different calculations.

Table 1 also presents the Cr and Os magnetic moments obtained from the sum rules applied to the theoretically calculated XAS and XMCD spectra. The XMCD sum rules are derived within an ionic model using a number of approximations [75]. It is well known than the application of the sum rules sometimes results in an error up to 50% [76]. However, we found relatively good agreement between the theoretically calculated magnetic moments in the frame of band theory and derived from the theoretical XAS and XMCD spectra using the sum rules.

Finally, our calculations produce induced spin and orbital magnetic moments at the oxygen site in SCOsO of about –0.085 μ_B and –0.006 μ_B, respectively. Going from SCOsO to the SCOsO/BTO heterostructure the spin and orbital magnetic moments increase in absolute value both at the Cr and Os sites (Table 1), and decrease in absolute value at the oxygen site. The spin magnetic moments change to 2.539 μ_B and 2.472 μ_B at the Cr site and to –1.662 μ_B and –1.558 μ_B at the Os site in the $[SCOsO/BTO]_{1\times1\times2}$ and $[SCOsO/BTO]_{2\times2\times1}$ heterostructures, respectively. We can conclude that both the spin and orbital magnetic moments are changed only slightly in different heterostructures. The hybridization between Ti and other transition metals *d* states plays an important role in the formation of the band structure of SCOsO/BTO heterostructures. It leads to induced spin and orbital magnetic moments at the Ti sites. The Sr and Ba sites also possess small induced spin and orbital magnetic moments (see Table 1).

4. Physical properties

4.1. Optical and MO properties

Among various properties of crystalline solids, the optical response to incident light is one of the standard phenomena used to characterize materials. Figure 4 shows the experimentally measured [77] diagonal optical reflectivity spectra (the upper panel) and dielectric functions ε_{1xx} (the middle panel) and ε_{2xx} (the lower panel) of BTO and the spectra calculated by the spin-polarized fully relativistic LMTO method in the GGA+SO+OP approximation for BTO, the SCOsO double perovskite, the SCOsO/BTO monolayered (1×1×1) and (1×1×2) supercell heterostructures. In the following, ε_{1xx} and ε_{2xy} denote the dispersive

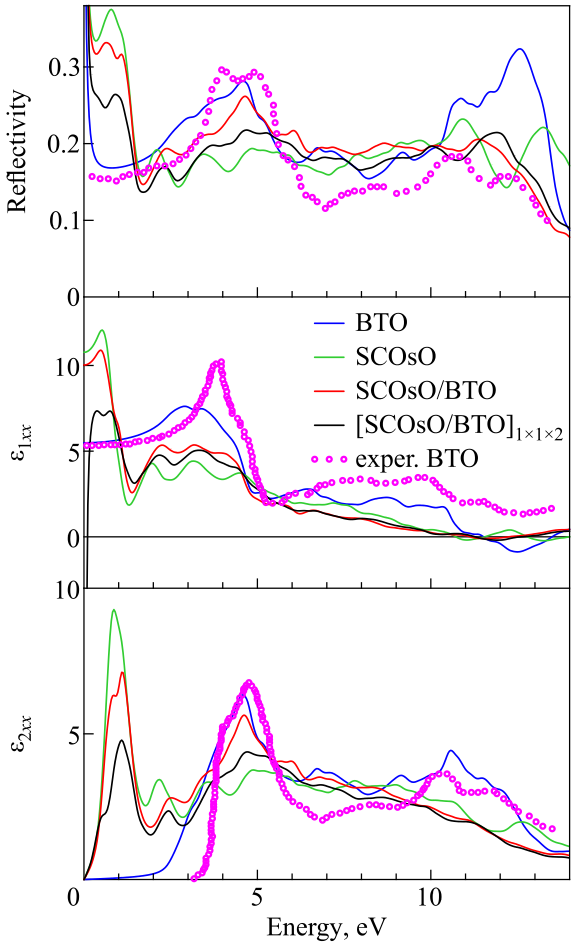

Fig. 4. (Color online) The experimentally measured [77] diagonal optical reflectivity spectra (upper panel) and dielectric functions ε_{1xx} (middle panel), and ε_{2xx} (lower panel) of BTO (open magenta circles) and the spectra calculated in the GGA+SO+OP approximation for BTO (blue curves), the SCOsO double perovskite (green curves), SCOsO/BTO monolayered (1×1×1) heterostructure (red curves) and (1×1×2) supercell heterostructure (black curves).

and absorptive parts, respectively, of the complex diagonal dielectric function $\varepsilon_{xx} = \varepsilon_{1xx} + i\varepsilon_{2xx}$.

Optical interband transitions in BTO take place from nine valence bands derived from O 2*p* orbitals separated by a direct gap of 2.35 eV at the Γ point to the Ti 3*d*-derived conduction bands (the upper panel of Fig. 2). The energy gap is somewhat lower than the experimental band gap of 3.2 eV for BTO [78]. The origin of this discrepancy may be the GGA approximation which underestimates the band gaps even for insulators. Our theoretical calculations are in good agreement with previous calculations [77, 79, 80] and describe well the shape and energy positions of the major peaks in the optical reflectivity spectrum as well as in the dielectrical functions ε(ω). However, due to underestimation of the energy gap, the optical absorption starts at smaller energies in our calculations in comparison with the experimental data (see the lower panel of Fig. 4). It also

affects the low energy part of the $\varepsilon_{1xx}(\omega)$ function from 3 to 4 eV (the middle panel of Fig. 4).

The optical reflectivity spectrum of the SCOsO double perovskite has several local minima at 1.8 eV, 2.8 eV, and 4 V and a strong reflective peak at 0.9 eV, which is absent in the optical reflectivity spectrum of BTO. The absorptive part of the dielectric function, $\varepsilon_{2xx}(\omega)$, shows a strong peak at around 1 eV and a smaller peak at 2.2 eV. Both peaks are absent in the absorptive part of the dielectric function of BTO and originate from the interband transitions between the energy bands in the close vicinity of the Fermi level (see Fig. 2). Figure 4 also presents the optical spectra for the SCOsO/BTO monolayered (1×1×1) and (1×1×2) supercell heterostructures. We found that the energy position of the major fine structures in the optical spectra for SCOsO and the heterostructures are pretty the same. However, the intensity of the major low energy peak at around 1 eV is significantly reduced going from SCOsO to the (1×1×1) and (1×1×2) heterostructures.

It is interesting to note that the major peak in the absorptive part of the dielectric function, $\varepsilon_{2xx}(\omega)$, at around 5 eV observed experimentally in BTO (the lower panel of Fig. 4) is well described by the theoretically calculated BTO spectrum as well as the spectrum for the SCOsO/BTO monolayered (1×1×1) heterostructure. The other two spectra, for pure SCOsO and the (1×1×2) supercell heterostructure, have lower intensity.

Figure 5 shows the theoretical Kerr rotation spectra (a) and Kerr ellipticity (b) of the SCOsO double perovskite, the SCOsO/BTO monolayered (1×1×1) and (1×1×2) supercell heterostructures calculated in the GGA+SO+OP approximation. Kerr rotation is quite large in SCOsO and the heterastructures. The characteristic features of the Kerr rotation spectrum in SCOsO are a sharp positive peak in the IR spectral range at ~ 0.15 eV, a negative minimum of around 0.5° at 1.2 eV, two strong prominent positive peaks with more than 1° amplitude situated between 1.6 and 2.5 eV with a local minimum in-between at 2.05 eV, and another strong positive peak of 1.2° at 3.1 eV followed by smaller negative and positive peaks at 3.75 eV and 4.2 eV, respectively. The Kerr spectra in the (1×1×1) and (1×1×2) heterostructures differ from the SCOsO Kerr spectrum in small details. In the IR spectral range below 1 eV the Kerr spectrum for the (1×1×1) heterostructure has much smaller and broader fine structures. The (1×1×2) heterostructure has an additional negative peak at 0.1 eV and two negative peaks at 1.05 eV and 1.3 eV. The peaks above 2.5 eV have a UV shift in both heterastructures in comparison with the Kerr spectrum in the SCOsO perovskite.

Essential points of the experimental Kerr ellipticity spectrum in SCOsO are zero-crossings at 0.15 eV and around 1.2 eV (that correspond to the 0.15 eV and 1.2 eV peaks in the Kerr rotation) with a broad positive structures between them, a prominent negative minimum at ~ 1.4 eV and several positive peaks above 1.8 eV. As in the Kerr rotation, the ellipticity peaks above 2.5 eV have an UV shift in both heterastructures in comparison with the ellipticity spectrum in SCOsO. The (1×1×2) heterostructure has an additional negative peak at 0.1 eV. The intensity of the prominent peak at 1.4 eV is significantly increased in the ellipticity spectra for both heterostructures in comparison with the SCOsO ellipticity spectrum.

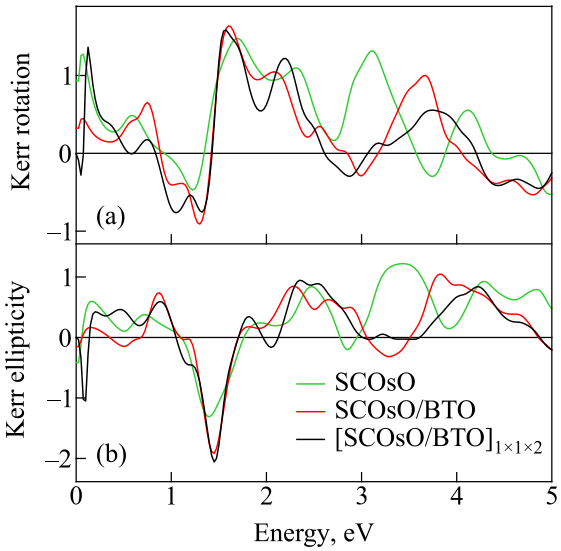

Fig. 5. (Color online) The theoretical Kerr rotation spectra (a) and Kerr ellipticity (b) of the SCOsO double perovskite (green curves), SCOsO/BTO monolayered (1×1×1) heterostructure (red curves) and (1×1×2) supercell heterostructure (black curves) calculated in the GGA+SO+OP approximation.

4.2. XMCD spectra

The XMCD is a powerful tool to study the element-specific local magnetic interactions and also it reflects the spin and orbital polarizations of the local electronic states. The XMCD experiments measure the difference of the x-rays absorption with opposite (left and right) directions of circular polarization. At first we consider the XAS and XMCD properties of the ions which become magnetic in the SCOsO/BTO heterostructure, namely, Ti and Ba.

The XAS of the ferroelectric barium titanate BTO at the Ti $L_{2,3}$ edges have been investigated experimentally, as well as theoretically by several authors [81–83]. Figure 6 (the upper panel) presents the experimental x-ray absorption spectrum [81] at the Ti $L_{2,3}$ edges in BTO compared with the theoretically calculated ones for BTO and the SCOsO/BTO heterostructure. The lower panel of Fig. 5 shows the theoretically calculated XMCD spectrum at the Ti $L_{2,3}$ edges in the SCOsO/BTO heterostructure. The experimentally measured Ti $L_{2,3}$ XAS consist of four major peaks in the range of 455–466 eV. The two peaks with lower energy are Ti L_3 edge peaks while the two peaks with higher energy are Ti L_2 edge peaks. It is well known that when a Ti ion is octahedrally coordinated, its two L_3 and L_2 peaks split into two separate e_g and t_{2g} peaks [84].

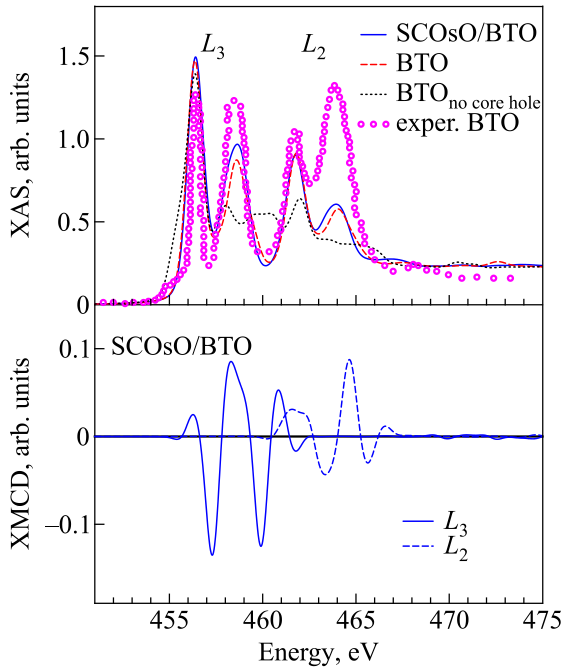

Fig. 6. (Color online) Upper panel: the experimental x-ray absorption spectrum [81] (open circles) at the Ti $L_{2,3}$ edges in BTO compared with the theoretically calculated ones for BTO with (dashed red curve) and without (dotted black curve) taking into account the core-hole effect, as well as for the SCOsO/BTO heterostructure (full blue curve). Lower panel: the theoretically calculated XMCD spectrum at the Ti $L_{2,3}$ edges in the SCOsO/BTO heterostructure.

The separation between these e_g and t_{2g} peaks is associated with the crystal-field splitting modified by the exchange interaction. Because the SO splitting of the core Ti $2p$ level (ΔE_{SO} = 5.74 eV) and the Ti $3d$ crystal-field splitting modified by the exchange interaction (ΔE_{CF} = 3.3 eV) are of the same order of magnitude the L_3 and L_2 x-ray absorption spectra are strongly overlapped. The four experimentally observed intense peaks from 455 to 466 eV can be, to a first approximation, assigned to $2p_{3/2} \to e_g$, $2p_{3/2} \to t_{2g}$, $2p_{1/2} \to e_g$, and $2p_{1/2} \to t_{2g}$ transitions, respectively. However, the $2p_{1/2} \to e_g$ and $2p_{1/2} \to t_{2g}$ transitions (L_2 spectrum) contribute also to the two low energy peaks.

As expected from Ti^{4+} ions and their octahedral coordination, BTO and the SCOsO/BTO heterostructure have similar spectra, as shown in Fig. 5. This demonstrates that there is no difference in the chemical environment of Ti ions. For the whole multilayered films, the Ti^{4+} ions are in octahedral coordination with oxygen, with all octahedra sharing corners. The theory reproduces the energy position of all fine structures quite well, however, it does not reproduce the experimentally observed L_3/L_2 x-ray absorption ratio. It is well known that the L_2 and L_3 absorption channels in early $3d$ transition metals with nearly empty d bands are strongly coupled through the photoelectron-core-hole Coulomb and exchange interactions [85–88]. This leads to the L_3/L_2 branching ratio close to 1:1, far from the statistical ratio 2:1, which is obtained in the single-particle theory unless the SO interaction in the final $3d$ band is considered. From our band structure calculations we obtained the L_3/L_2 branching ratio equal to 1.65, which is far from the experimentally observed. This problem can be accounted for through many-electron calculations and we address it for future investigations.

We investigated the core-hole effect in the final state using the supercell approximation where the excited atom is formally treated as an impurity. We found that the core-hole interaction strongly influences Ti empty $3d$ states: they become much more narrow and shift downward by ~ 2.4 eV (see Fig. 7). The core-hole interaction significantly improves the agreement between theoretically calculated and experimentally measured Ti $L_{2,3}$ XAS in BTO (the upper panel in Fig. 6). The theory reproduces well the widths of all four major peaks in the x-ray absorption. After taking into account the core-hole effect we obtained the L_3/L_2 branching ratio equal to 1.2, which is in much better agreement with the experiment.

Pure BTO possesses no dichroism because all the ions in BTO are nonmagnetic. However, due to the hybridization between Ti d states and Cr/Os d states in the SCOsO/BTO heterostructures there are induced spin and orbital magnetic moments at the Ti sites (see Table 1). Therefore, one would expect a well pronounced XMCD signal at the Ti $L_{2,3}$ edges (the lower panel of Fig. 6). The experimental measurements of the XMCD spectra at Ti $L_{2,3}$ edges in SCOsO/BTO are highly desirable.

The XAS of the ferroelectric barium titanate BTO at the Ba L_3 edge have been investigated experimentally, as well as theoretically by several authors [89–94]. Figure 8 shows

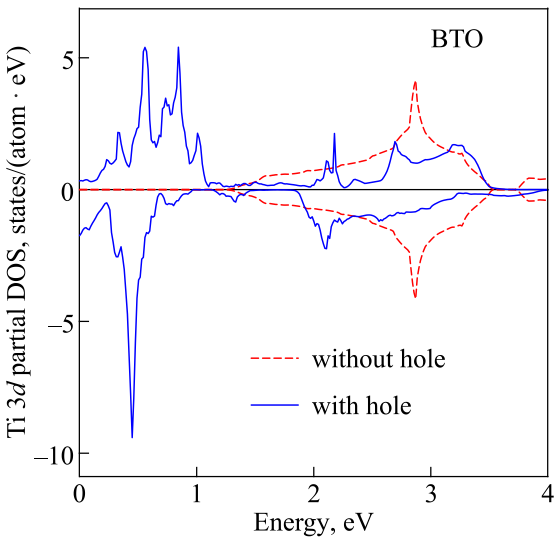

Fig. 7. (Color online) The Ti $3d$ partial density of states [in states/(atom·eV)] calculated for BTO with (full blue curve) and without (dashed red curve) taking into account a core-hole at the Ti $2p_{3/2}$ core level.

the experimental x-ray absorption spectrum [89] at the Ba L_3 edge in BTO compared with the theoretically calculated ones for BTO and the SCOsO/BTO heterostructure. The lower panel of Fig. 8 presents the theoretically calculated XMCD spectrum in the SCOsO/BTO heterostructure at the Ba L_3 edge. On the basis of the dipole selection rule, the large white line in BTO at around 5249 eV is ascribed to the resonant excitation from Ba $2p_{3/2}$ to Ba $5s$ and $5d$ unoccupied states. The low- and high-energy regions could be tentatively attributed to the hybridization of Ba $5d$ and O $2p$ orbitals. The spectrum was calculated with taking into account a Ba $2p_{3/2}$ core hole and convoluted by a 1 eV Lorentzian contribution accounting for the core-hole lifetime broadening. We found that the core-hole effect has a small influence on the shape of the Ba L_3 x-ray absorption spectrum. The theoretically calculated spectrum reproduces well the overall profile, including the low- and high-energy regions noted above and the small peaks at the high energies above the white line. Yoshii *et al.* [94] show that Ba L_3 XAS reveals no apparent change between the room temperature paraelectric cubic phase and the ferroelectric tetragonal phase at 150° C. On the basis of the discussion in Ref. 95, the absence of temperature dependence of the spectrum implies the absence of atomic displacements around Ba^{2+} ions. The Ba L_3 x-ray absorption spectra also have almost the same shape in pure BTO and in the SCOsO/BTO heterostructure. The high energy shoulders at around 5251.5 eV and 5253.5 eV are better pronounced in the heterostructure.

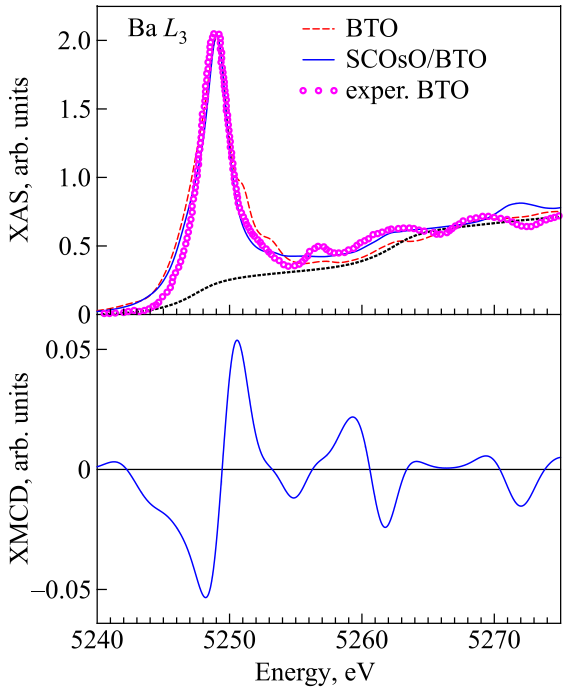

Fig. 8. (Color online) Upper panel: the experimental x-ray absorption spectrum [89] (open circles) at the Ba L_3 edge in BTO compared with the theoretically calculated ones for BTO (dashed red curve) and the SCOsO/BTO heterostructure (full blue curve). Lower panel: the theoretically calculated XMCD spectrum for the SCOsO/BTO heterostructure at the Ba L_3 edge.

Figure 9 shows the calculated XAS and XMCD spectra at the Os $L_{2,3}$ edges in the SCOsO double perovskite and SCOsO/BTO heterostructure together with the experimental spectra for SCOsO [24]. The theoretically calculated Os L_2 and L_3 XAS for these structures have a high resemblance to each other. The theory reproduces well the shape of the Os $L_{2,3}$ x-ray absorption spectra. The XAS at the L_3 and L_2 edges in the SCOsO/BTO heterostructure possess an additional high energy peak shifted by approximately 15 eV from the major absorption peak.

The lower panels in Fig. 9 present the experimental XMCD [24] at the Os $L_{2,3}$ edges in SCOsO compared with the theoretically calculated ones for SCOsO and the SCOsO/BTO heterostructure. The Os L_3 XMCD spectrum is positive and has a double peak structure. The dichroism at the Os L_2 edge is much stronger and has an opposite sign in comparison with the L_3 XMCD spectrum. The theory reproduces well the shape of the Os $L_{2,3}$ XMCD spectra in the SCOsO double perovskite. The theoretically calculated Os L_3 spectrum in the SCOsO/BTO heterostructure has a more intensive high energy peak in comparison with SCOsO.

The XAS and XMCD spectra at the Cr $L_{2,3}$ edges are very similar for the SCOsO double perovskite and SCOsO/BTO heterostructures (not shown). We can conclude that the presence of the BTO layer in the SCOsO/BTO heterostructures only moderately changes the magnetic structure of the SCOsO layer.

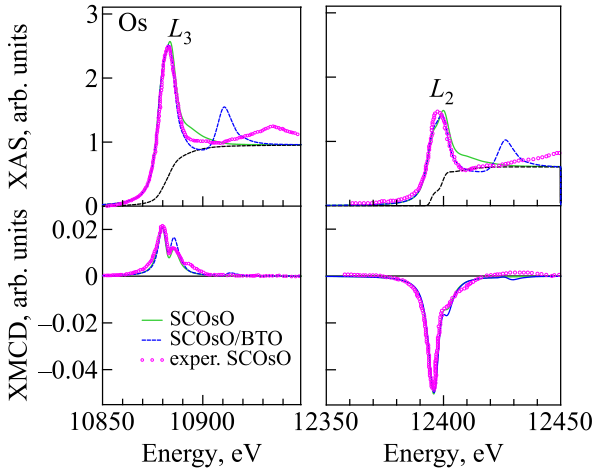

Fig. 9. (Color online) Upper panel: the experimental x-ray absorption spectra [24] (open circles) at the Os $L_{2,3}$ edges in SCOsO compared with the theoretically calculated ones for SCOsO (full green curves) and the SCOsO/BTO heterostructure (dashed blue curves). Lower panel: the experimental XMCD [24] (open circles) at the Os $L_{2,3}$ edges in SCOsO compared with the theoretically calculated ones for SCOsO (full green curves) and the SCOsO/BTO heterostructure (dashed blue curves).

5. Conclusions

The combination of several physical properties such as superconductivity, ferro- and antiferro-magnetism, ferroelectricity, or even multiferroicity in artificial heterostructures paves the way to a rich variety of interesting new physics and novel concepts in condensed matter physics. Oxide thin films and their artificial heterostructures are at the forefront of modern materials science due to an enormous progress in oxide thin film technology. Along with that they have outstanding physical properties.

In this work we present a systematic study of the electronic structure and physical properties of the SCOsO/BTO heterostructures using the fully relativistic spin-polarized Dirac linear muffin-tin orbital band-structure method in the GGA approximation. The ground state band structure of SCOsO with the SO coupling has a semimetal character. To obtain the insulating ground state observed experimentally [24] one has to take into account the OP correction. We applied intra-atomic Coulomb repulsion U on the Os ion using the LSDA+SO+OP method (with $U_{\text{eff}} = U - J = 0$ eV) to obtain the insulating solution. Therefore, the opening of the gap in SCOsO is not such as in a Mott insulator (it is a band insulator), but rather as an "energy gap correction" to GGA. The GGA+SO+OP approach produces the insulating solution for SCOsO and the SCOsO/BTO, $[SCOsO/BTO]_{1\times1\times2}$ heterostructures, however, the $[SCOsO/BTO]_{2\times2\times1}$ heterostructure is a semimetal with very small DOS at the Fermi level.

First principles calculations predict that SCOsO as well as the SCOsO/BTO heterostructures are (without considering the SO coupling) actually ferrimagnetic with precisely compensating spin moments, or spin-asymmetric compensated semiconductor ferrimagnets in which the electrons and holes are each fully polarized and have opposite spin directions, in spite of a zero net moment and hence no macroscopic magnetic field. The SO coupling degrades this by giving a nonzero total moment, but the band structure is little changed. Therefore, the saturation moments of ferrimagnetic SCOsO and the SCOsO/BTO heterostructures are entirely due to the SO coupling.

The element-specific x-ray absorption spectra and x-ray magnetic circular dichroism at the Ti, Ba, and Os $L_{2,3}$ edges in SCOsO and the SCOsO/BTO heterostructures were investigated theoretically from first principles. The theory describes rather well the shape and relative intensities of the x-ray absorption and XMCD spectra in SCOsO and BTO. The final-state interaction improves the agreement between the theory and the experiment at the Ti $L_{2,3}$ edges, however, it has a minor influence on the shape of the Ba and Os $L_{2,3}$ x-ray absorption spectra.

Artificial oxide heterostructures are particularly promising for the realization of materials with improved and new functionalities and novel device concepts. Due to the complexity of the involved oxide materials, the rich variety of physics is far from being understood and needs further detailed studies. Moreover, intermixing of the different atomic species deposited in multilayer structures plays an important role and might influence or even dominate the overall physical properties. Therefore, a careful investigation of the electronic structure, optical, and element-specific XMCD properties of artificially constructed material systems is highly desirable.

1. I. E. Dzyaloshinskii, *Sov. Phys. JETP* **10**, 628 (1959).
2. D. N. Astrov, *Sov. Phys. JETP* **11**, 708 (1960).
3. H. Schmid, *Ferroelectrics* **162**, 317 (1994).
4. T. Kimura, T. Goto, K. Thizaka, T. Arima, and Y. Tokura, *Nature* **426**, 55 (2003).
5. T. Lottermoser, T. Lonkai, U. Amann, D. Hohlwein, J. Ihringer, and M. Fiebig, *Nature* **430**, 541 (2003).
6. T. Lottermoser, H. Yamada, J. Matsuno, T. Arima, M. Kawasaki, and Y. Tokura, *J. Magn. Magn. Mater.* **310**, 2204 (2007).
7. J. T. Heron, D. G. Schlom, and R. Ramesh, *Appl. Phys. Rev.* **1**, 021303 (2014).
8. C.-W. Nan, M.-I. Bichurin, S. Dong, D. Viehland, and G. Srinivasan, *J. Appl. Phys.* **103**, 031101 (2008).
9. N. A. Hill, *J. Phys. Chem. B* **104**, 6694 (2000).
10. C. W. Nan, G. Liu, Y. Lin, and H. Chen, *Phys. Rev. Lett.* **94**, 197203 (2005).
11. P. R. Maiti and D. Chakravorty, *Trans. Indian Ceram. Soc.* **70**, 53 (2011).
12. R. V. Chopdekar and Y. Suzuki, *Appl. Phys. Lett.* **89**, 182506 (2006).
13. M. K. Lee, T. K. Nath, C. B. Eom, M. C. Smoak, and F. Tsui, *Appl. Phys. Lett.* **77**, 3547 (2000).
14. D. Dale, A. Fleet, J. D. Brock, and Y. Suzuki, *Appl. Phys. Lett.* **82**, 3725 (2003).
15. W. Eerenstein, M. Wiora, J. L. Prieto, J. F. Scott, and N. D. Mathur, *Nat. Mater.* **6**, 348 (2007).
16. H. F. Tian, T. L. Qu, L. B. Luo, J. J. Yang, S. M. Guo, H. Y. Zhang, Y. G. Zhao, and J. Q. Li, *Appl. Phys. Lett.* **92**, 063507 (2008).
17. C. A. F. Vaz, J. Hoffman, A.-B. Posadas, and C. H. Ahn, *Appl. Phys. Lett.* **94**, 022504 (2009).
18. K. I. Kobayashi, T. Kimura, H. Sawada, K. Terakura, and Y. Tokura, *Nature* **395**, 677 (1998).
19. H. Kato, T. Okuda, Y. Okimoto, Y. Tomioka, K. Oikawa, T. Kamiyama, and Y. Tokura, *Phys. Rev. B* **69**, 184412 (2004).
20. J. M. D. Coey, *Adv. Phys.* **48**, 167 (1999).
21. D. Serrate, J. M. D. Teresa, and M. R. Ibarra, *J. Phys. Condens. Matter* **19**, 023201 (2007).
22. J. B. Philipp, P. Majewski, L. Alff, A. Erb, R. Gross, T. Graf, M. S. Brandt, J. Simon, T. Walther, W. Mader, D. Topwal, and D. D. Sarma, *Phys. Rev. B* **68**, 144431 (2003).
23. H. Kato, T. Okuda, Y. Okimoto, Y. Tomioka, K. Oikawa, T. Kamiyama, and Y. Tokura, *Phys. Rev. B* **65**, 144404 (2002).
24. Y. Krockenberger, K. Mogare, M. Reehuis, M. Tovar, M. Jansen, G. Vaitheeswaran, V. Kanchana, F. Bultmark, A. Delin, F. Wilhelm, A. Rogalev, A. Winkler, and L. Alff, *Phys. Rev. B* **75**, 020404(R) (2007).
25. M. I. Friezer, *IEEE Trans. Magn.* **4**, 152 (1968).
26. J. B. Kortight and S.-K. Kim, *Phys. Rev. B* **62**, 12216 (2000).

27. G. Y. Guo, H. Ebert, W. M. Temmerman, and P. J. Durham, *Phys. Rev. B* **50**, 3861 (1994).
28. V. N. Antonov, A. I. Bagljuk, A. Y. Perlov, V. V. Nemoshkalenko, V. N. Antonov, O. K. Andersen, and O. Jepsen, *Fiz. Nizk. Temp.* **19**, 689 (1993) [*Low Temp. Phys.* **19**, 494 (1993)].
29. L. A. Shebanov, *Phys. Status Solidi A* **65**, 321 (1981).
30. M. Opel, S. Gergäs, E. P. Menzel, A. Nielsen, D. Reisinger, K.-W. Nielsen, A. Brandlmaier, F. D. Czeschka, M. Althammer, M. Weiler, S. T. B. Goennenwein, J. Simon, M. Svete, W. Yu, S.-M. Hühne, W. Mader, and R. Gross, *Phys. Status Solidi A* **208**, 232 (2011).
31. H. F. Kay and P. Vousden, *Philos. Mag.* **40**, 1019 (1949).
32. V. N. Antonov, M. Galli, F. Marabelli, A. N. Yaresko, A. Y. Perlov, and E. Bauer, *Phys. Rev. B* **62**, 1742 (2000).
33. V. N. Antonov, B. N. Harmon, and A. N. Yaresko, *Phys. Rev. B* **63**, 205112 (2001).
34. V. N. Antonov, B. N. Harmon, A. N. Yaresko, and A. P. Shpak, *Phys. Rev. B* **75**, 184422 (2007).
35. V. N. Antonov, A. N. Yaresko, and O. Jepsen, *Phys. Rev. B* **81**, 075209 (2010).
36. B. J. Ruck, H. J. Trodahl, J. H. Richter, J. C. Cezar, F. Wilhelm, A. Rogalev, V. N. Antonov, B. D. Le, and C. Meyer, *Phys. Rev. B* **83**, 174404 (2011).
37. L. Uba, S. Uba, L. P. Germash, L. V. Bekenov, and V. N. Antonov, *Phys. Rev. B* **85**, 125124 (2012).
38. V. N. Antonov, D. A. Kukusta, S. V. Moklyak, D. V. Mazur, and L. V. Bekenov, *Phys. Rev. B* **101**, 054441 (2020).
39. O. K. Andersen, *Phys. Rev. B* **12**, 3060 (1975).
40. A. Y. Perlov, A. N. Yaresko, and V. N. Antonov, *PY-LMTO, A Spin-polarized Relativistic Linear Muffin-tin Orbitals Package for Electronic Structure Calculations* (1995), *unpublished*.
41. V. V. Nemoshkalenko, A. E. Krasovskii, V. N. Antonov, Vl. N. Antonov, U. Fleck, H. Wonn, and P. Ziesche, *Phys. Status Solidi B* **120**, 283 (1983).
42. J. P. Perdew and Y. Wang, *Phys. Rev. B* **45**, 13244 (1992).
43. J. P. Perdew, K. Burke, and M. Ernzerhof, *Phys. Rev. Lett.* **77**, 3865 (1996).
44. P. E. Blöchl, O. Jepsen, and O. K. Andersen, *Phys. Rev. B* **49**, 16223 (1994).
45. J. L. Campbell and T. Parr, *At. Data Nucl. Data Tables* **77**, 1 (2001).
46. K. Lie, R. Hoier, and R. Brydson, *Phys. Rev. B* **61**, 1786 (2000).
47. S.-D. Mo and W. Y. Ching, *Phys. Rev. B* **62**, 7901 (2000).
48. S.-D. Mo and W. Y. Ching, *Appl. Phys. Lett.* **78**, 3809 (2001).
49. Y.-N. Xu, Y. Chen, S.-D. Mo, and W. Y. Ching, *Phys. Rev. B* **65**, 235105 (2002).
50. W. Y. Ching, S.-D. Mo, and Y. Chen, *J. Am. Ceram. Soc.* **85**, 11 (2002).
51. T. Mizoguchi, I. Tanaka, S. Yoshioka, M. Kunisu, T. Yamamoto, and W. Y. Ching, *Phys. Rev. B* **70**, 045103 (2004).
52. H. Ikeno and T. Mizoguchi, *Microscopy* **66**, 305 (2017).
53. M. S. S. Brooks and B. Johansson, *Handbook of Magnetic Materials*, K. H. J. Buschow (ed.), North-Holland, Amsterdam (1993), Vol. 7, p. 139.
54. M. S. S. Brooks, *Physica B* **130**, 6 (1985).
55. O. Eriksson, M. S. S. Brooks, and B. Johansson, *Phys. Rev. B* **41**, 7311 (1990).
56. L. Severin, M. S. S. Brooks, and B. Johansson, *Phys. Rev. Lett.* **71**, 3214 (1993).
57. A. Mavromaras, L. Sandratskii, and J. Kübler, *Solid State Commun.* **106**, 115 (1998).
58. V. Antonov, B. Harmon, and A. Yaresko, *Electronic Structure and Magneto-Optical Properties of Solids*, Kluwer, Dordrecht (2004).
59. G. Vignale and M. Rasolt, *Phys. Rev. Lett.* **59**, 2360 (1987).
60. P. Skudlarski and G. Vigmale, *Phys. Rev. B* **48**, 8547 (1993).
61. M. Higuchi and A. Haegawa, *J. Phys. Soc. Jpn.* **66**, 149 (1997).
62. S. V. Beiden, W. M. Temmerman, Z. Szotek, and G. A. Gehring, *Phys. Rev. Lett.* **79**, 4970 (1997).
63. I. V. Solovyev, A. I. Liechtenstein, and K. Terakura, *Phys. Rev. Lett.* **80**, 5758 (1998).
64. A. N. Yaresko, V. N. Antonov, and P. Fulde, *Phys. Rev. B* **67**, 155103 (2003).
65. V. N. Antonov and L. V. Bekenov, *Fiz. Nizk. Temp.* **43**, 724 (2017) [*Low Temp. Phys.* **43**, 578 (2017)].
66. A. R. Mackintosh and O. K. Andersen, *Electrons at the Fermi Surface*, M. Springford (ed.), Cambridge University Press, Cambridge (1980), p. 149.
67. B. C. Jeon, C. H. Kim, S. J. Moon, W. S. Choi, H. Jeong, Y. S. Lee, J. Yu, C. J. Won, J. H. Jung, N. Hur, and T. W. Noh, *J. Phys. Condens. Matter* **22**, 345602 (2010).
68. K.-W. Lee and W. E. Pickett, *Phys. Rev. B* **77**, 115101 (2008).
69. H. Das, M. D. Raychaudhury, and T. Saha-Dasgupta, *Appl. Phys. Lett.* **92**, 201912 (2008).
70. G. G. Scott, *J. Phys. Soc. Jpn.* **17**, 372 (1962).
71. W. Marshall and S. W. Lovsey, *Theory of Thermal Neutron Scattering*, Oxford University Press, Oxford (1971).
72. M. Blume, *J. Appl. Phys.* **57**, 3615 (1985).
73. B. T. Thole, P. Carra, F. Sette, and G. van der Laan, *Phys. Rev. Lett.* **68**, 1943 (1992).
74. P. Carra, B. T. Thole, M. Altarelli, and X. Wang, *Phys. Rev. Lett.* **70**, 694 (1993).
75. H. Ebert, *Rep. Prog. Phys.* **59**, 1665 (1996).
76. V. N. Antonov, O. Jepsen, A. N. Yaresko, and A. P. Shpak, *J. Appl. Phys.* **100**, 043711 (2006).
77. G. Gupta, T. Nautiyal, and S. Auluck, *Phys. Rev. B* **69**, 052101 (2004).
78. S. H. Wemple, *Phys. Rev. B* **2**, 2679 (1970).
79. D. Bagayoko, G. L. Zhao, J. D. Fan, and J. T. Wang, *J. Phys. Condens. Matter* **10**, 5645 (1998).
80. S. Saha, T. P. Sinha, and A. Mookerjee, *Phys. Rev. B* **62**, 8828 (2000).
81. J. Zhang, A. Visinoiu, F. Heyroth, F. Syrowatka, M. Alexe, D. Hesse, and H. S. Leipner, *Phys. Rev. B* **71**, 064108 (2005).
82. A. Chasse, S. Borek, K.-M. Schindler, M. Trautmann, M. Huth, F. Steudel, L. Makhova, J. Gräfe, and R. Denecke, *Phys. Rev. B* **84**, 195135 (2011).
83. G. Liu, Y. Wang, B. Zou, W. Liang, N. M. Alford, D. W. McComb, and P. K. Petrov, *J. Phys. Chem. C* **120**, 16681 (2016).

84. A. S. Sefat, G. Amow, M. Y. Wu, G. A. Botton, and J. E. Greedan, *J. Solid State Chem.* **178**, 1008 (2005).
85. J. Zaanen, G. A. Sawatzky, J. Fink, W. Speier, and J. C. Fuggle, *Phys. Rev. B* **32**, 4905 (1985).
86. J. Schwitalla and H. Ebert, *Phys. Rev. Lett.* **80**, 4586 (1998).
87. P. Krüger and C. R. Natoli, *Phys. Rev. B* **70**, 245120 (2004).
88. A. L. Ankudinov, A. I. Nesvizhskii, and J. J. Rehr, *Phys. Rev. B* **67**, 115120 (2003).
89. K. Yoshii, I. Jarrige, C. Suzuki, D. Matsumura, Y. Nishihata, Y. Yoneda, T. Fukuda, K. Tamura, Y. Ito, T. Mukoyama, T. Tochio, H. Shinotsuka, and S. Fukushima, *J. Phys. Chem. Solids* **73**, 1106 (2012).
90. K. Asokan, J. C. Jan, J. W. Chiou, W. F. Pong, P. K. Tseng, and I. N. Lin, *J. Synchrotron Radiat.* **8**, 839 (2001).
91. K. Asokan, J. C. Jan, J. W. Chiou, W. F. Pong, M.-H. Tsai, H. L. Shih, H. Y. Chen, H. C. Hsueh, C. C. Chuang, Y. K. Chang, Y. Y. Chen, and I. N. Lin, *J. Phys. Condens. Matter* **13**, 11087 (2001).
92. Y.-H. Tang, M.-H. Tsai, J. Jan, and W. Pong, *Chin. J. Phys.* **41**, 167 (2003).
93. M. Hidaka, N. Tokiwa, S. Takahashi, J.-Y. Choi, and J. M. Lee, *Phys. Status Solidi B* **241**, 1058 (2004).
94. K. Yoshii, Y. Yoneda, I. Jarrige, T. Fukuda, Y. Nishihata, C. Suzuki, Y. Ito, T. Terashima, S. Yoshikado, and S. Fukushima, *J. Phys. Chem. Solids* **75**, 339 (2014).
95. R. E. Cohen and H. Krakauer, *Phys. Rev. B* **42**, 6416 (1990).

Електронна структура та фізичні властивості гібридних гетероструктур $Sr_2CrOsO_6/BaTiO_3$

V. N. Antonov, L. V. Bekenov

Представлено електронні спектри та магнітні властивості гібридних гетероструктур, що поєднують феромагнітний подвійний перовскіт Sr_2CrOsO_6 (SCOsO) та сегнетоелектрик $BaTiO_3$ (BTO), які розраховані в підході GGA із використанням повністю релятивістського спінополяризованого методу LMTO Дірака. Структура електронних смуг вивчається в оксидах BTO та SCOsO, а також у гетероструктурах SCOsO/BTO із різними суперелементами: (1×1×1) одношарових, (2×2×1) та (1×1×2) SCOsO/BTO гетероструктур. Оптичні та магнітооптичні спектри чистих оксидів BTO та SCOsO, а також SCOsO/BTO гетероструктур досліджуються теоретично та порівнюються з доступними експериментальними даними. Теоретично досліджено спектри специфічного поглинання рентгенівських променів, а також рентгенівський магнітний круговий дихроїзм на $L_{2,3}$ ребрах Ti, Ba та Os у SCOsO/BTO гетероструктурах. Виявлено добру згоду з експериментальними спектрами.

Ключові слова: електронна структура, магнітний момент, рентгенівський магнітний циркулярний дихроїзм, діелектрична функція, обертання Керра, гетероструктури, мультифероїки.